Influence of the Incidence Angle of Sputtered Particles on the Surface, Interface, and Magnetic Properties of Fe/Si Multilayers Deposited by DC Magnetron Sputtering Technique with Large-Area Rectangular-Target

Simeng Xiang(项丝梦)[1], Zhong Zhang(张众)[1*], Fengrui Tang(汤丰锐)[1], Yibo Wang(王一博)[1], Zhanshan Wang(王占山)[1]

[1] MOE Key Laboratory of Advanced Micro-structured Materials, Institute of Precision Optical Engineering (IPOE), School of Physics Science and Engineering, Tongji University, Shanghai 200092, China

*Corresponding author. E-mail: zhangzhongcc@tongji.edu.cn

Abstract

Fe/Si multilayer are widely used in polarized-neutron applications because of their high theoretical polarization efficiency. Reducing interface roughness is critical for maintaining the polarization performance of Fe/Si multilayers. In this paper, the honeycomb mask was designed to limit large-angle incident particles during the large-area rectangular-target direct current magnetron sputtering for lower interface and surface roughness of Fe/Si multilayers. The surface and interface performance were charactered with grazing incidence X-ray reflectivity, X-ray diffuse scattering, atomic force microscope and optical profilometer (OP). Hysteresis loop was measured to characterize the magnetic properties. The Fe-on-Si/Si-on-Fe interface widths decreased from 0.79/0.58 nm to 0.53/0.45 nm according to fitted Grazing incidence X-ray reflectivity (GIXR) curves. The surface roughness was reduced from 0.29/0.67 nm RMS in AFM/OP to 0.16/0.39 nm. The Fe-on-Si/Si-on-Fe interface roughness decreased from 0.71/0.50 nm to 0.47/0.40 nm according to fitted X-ray diffuse scattering (XRS) curves. The coercivity decreased from 50 Oe to 25 Oe in hysteresis loop results. These results indicate that limiting large-angle incident particles can reduce the coercivity by improving the interface and surface quality without changing the crystallite size These results indicate that limiting large-angle incident particles can reduce the coercivity by improving the interface and surface quality without changing the crystallite size

Keywords: Fe/Si multilayer, honeycomb mask, roughness, magnetic properties

PACS: 68.55.-a, 75.70.-i, 81.15.-z, 28.20.-v

Introduction

Fe/Si multilayers have attracted broad interest for applications in neutron polarizing optics [1] and magnetoresistive devices [2], together with potential applications in spintronics and magnetic sensing [3]. Their properties are strongly influenced by interface structure and composition. Intermixing and silicide formation can modify the magnetic response and effective magnetic thickness of the Fe layers [4]. In neutron polarizing mirrors, interface imperfections also modify the scattering-length-density (SLD) profile and reflected intensity. Roughness contributes to diffuse scattering, while intermixing may reduce the SLD contrast between adjacent layers [1]. Control of surface morphology and interface formation is therefore important for achieving the desired structural and magnetic properties.

Many approaches have been explored to reduce interface and surface roughness of Fe/Si multilayer, such as reactive deposition, varying sputtering method, tuning Si or Fe layer thickness, employing slit structures, and adding interlayers. Zhang et al. varied the Si layer thickness in Fe/Si multilayers deposited by DC magnetron sputtering to change the interfacial structure and control interface roughness [5]. It was found that increasing the Si thickness reduced the Fe-on-Si interlayer thickness from 0.95 nm to 0.38 nm. This change shifted the interfaces from asymmetric to symmetric. Amir et al. compared the interfacial structures of Fe/Si multilayers prepared by electron-beam evaporation and DC magnetron sputtering [4]. They concluded that DC magnetron sputtering produced a thinner Fe–Si interlayer, which reduced interdiffusion and yielded smoother interfaces. Kumar et al. changed the Si layers thickness in Fe/Si multilayers to investigate the morphology of silicon on Fe interface [6]. They found that increasing the Si layer thickness decreased the peak intensity in the atomic force microscopy (AFM) images, and the surface became smoother and more uniform. Ashfaq et al. modified the aperture geometry in magnetron sputtering to change particle incidence and reduce interface roughness. [7]. They showed that the modified Fe sputtering aperture decreased the Fe–Si interlayer thickness and reduced its roughness. Kharmouche et al. deposited Fe films by thermal evaporation onto monocrystalline Si (100) and Si (111) substrates to examine the effect of substrate orientation on film roughness [8] They revealed that Fe films on Si (111) exhibited higher surface roughness than those on Si (111). Høghøj et al. used reactive sputtering of Si in N_2 to form a SiN_x interdiffusion barrier, which inhibited the formation of non-magnetic layers in Fe/Si multilayers [9]. Reflectivity and transmission results confirmed that this goal was achieved. Zubayer et al. inserted $^{11}B_4C$ interlayers into Fe/Si multilayers to improve interface quality and control diffusion for polarized neutron optics [10]. They showed that 1Å and 2Å $^{11}B_4C$ interlayers sharpened the interfaces, reduced the interface width, and suppressed excessive Si diffusion into the Fe layers. A. Zubayer revealed the incorporation of ^{11}B4C changed the Fe microstructure by suppressing crystallization [1]. The coercivity of Fe/Si multilayer was reduced and the magnetic properties were improved. The above researches

have been proved effective in reducing the interfacial roughness of Fe/Si multilayer. However, the application of the above methods might be limited because the adjustment of multilayer configuration or deposition system were often relied on. Although the incorporation of $^{11}B_4C$ can improve the interfacial quality and magnetic performance, thereby enhancing the polarization efficiency. The Fe/Si Multilayers with $^{11}B_4C$ is not suitable in neutron polarizing supermirrors because its relatively large neutron scattering cross section can introduce additional neutron losses. Therefore, the honeycomb mask is designed to limit the large-angle incident particles, thereby reducing the interface and surface roughness of Fe/Si multilayers.

Particle incidence angle affects the growth morphology of sputtered films. At oblique incidence, surface protrusions shadow neighboring regions and produce uneven deposition. If surface diffusion is insufficient to smooth these variations, shadowing can promote columnar growth and roughening. In magnetron-sputtered FeCoB films, increasing the incidence angle was associated with changes in surface roughness and magnetic anisotropy [11]. Increased substrate inclination also increased surface and interface roughness in Mo/Si multilayers, particularly at 50°-70° [12]. Conversely, collimating sputtered particles was shown to suppress interface roughness in multilayer mirror coatings [9]. These findings have motivated the present investigation of how restricting large-angle incident particles affects the surface, interface, and magnetic properties of Fe/Si multilayers.

In this paper, the honeycomb mask was designed to limit large-angle incident particles during depositing Fe/Si multilayers for smoother interfaces/surface and higher magnetic properties. In Section 2, the particle sputtering simulation was presented to evaluate the effect of honeycomb mask to limit the large-angle incident particles. Then, this honeycomb mask was applied to depositing the Fe/Si multilayer. In Section 3, the experiments of multilayer fabrication and characterization were described. The results were discussed in Section 4. The simulation results of the honeycomb mask were reported in Section 4.1. The interface width was evaluated by using XRR in Section 4.2. The surface roughness was measured in Section 4.3. The interface roughness was analyzed by using XRS in Section 4.4. In Section 4.5, the roughness evolution mechanism was investigated through X-ray diffraction (XRD). Finally, the magnetic properties of the Fe/Si multilayers were compared in Section 4.6.

2. Method

Large rectangular targets were employed to sputtering Fe/Si multilayers on large substrate. The target size was 130 mm (x direction) × 380 mm (y direction), and the distance between target and substrate was 115 mm. During DC magnetron sputtering with large-area rectangular targets, large-angle incident particles have lower mobility on the substrate surface. Therefore, Fe/Si multilayers deposited using large-area rectangular targets can exhibit greater interfacial and surface

roughness. Therefore, Fe/Si multilayers deposited using large-area rectangular targets can exhibit greater interfacial and surface roughness. [13].

Previous studies have shown that when the incidence angle exceeds 52°, surface roughness increases markedly [14]. The honeycomb mask was designed to block large-angle particles emitted from the target and to limit the incidence angle at the substrate to below 52°. As a result, large-angle particles cannot pass through the honeycomb openings to reach the substrate. According to the initial angle probability distribution in the literature, the size of honeycomb mask was 300 mm (x direction) × 400 mm (y direction) and the honeycomb diameter was set to 10mm and the thickness to 5mm [15-16].

To verify the angular distribution of incident particles, the Monte Carlo simulation was carried out with MATLAB [16-17]. *Based on the chamber dimensions and the particle transmission geometry, the mask was placed 40 mm from the substrate. This spacing provided the desired angular cutoff, thereby helping to reduce surface and interface roughness. When depositing multilayers using a linear direct current magnetron sputtering, the substrate moved horizontally in front of the target. The size of the target material we used was 130×380mm, and the size of the substrate was 300×200mm. Additionally, the center of the substrate was collinear with the center of the target. The distance between the target and the mask (d1) was 75 mm and the distance between mask and substrate (d2) was 40 mm. Under a sufficiently high vacuum, the particles emitted from the target follow a cosine distribution, and the deposition process is approximated by a collisionless with straight-line transport trajectory as shown in Fig. 1[17].*

The angular distribution of sputtered particles in magnetron sputtering was described by a modified cosine function [18]. The probability P(θ) for a particle emitted from a point on the target surface is expressed as: $P(\theta) = 2a \cdot cos\theta/a^2 + (1 - a^2)cos^2\theta$, where θ is the angle between the sputtered particle trajectory and the surface normal of the target [19]. This distribution forms an elliptical profile, and the parameter α determines the ratio of the major to minor axes of this ellipse [19]. The value of α depends on the target material and the plasma energy. It is expressed as $\alpha = E_{ion} * cos\theta_i/2U_b$, where E_{ion} is the plasma energy, U_b is the surface binding energy of the target material, and θ_i is the angle of plasma [20]. In sputtering, $U_b$is the minimum energy needed for an atom to leave the surface. In this paper, α of Fe target was set as 1.3 [21]. *The Monte Carlo simulation was performed for each case, with and without the honeycomb mask. Each simulation tracked 300000 sputtered particles generated from random positions on the target surface. The entire substrate area of 300 mm × 200 was divided into 5 mm × 5 mm cells, giving 2400 cells in total. Particle origins were randomly sampled over the target area, and emission directions were generated based on the cosine distribution. Each trajectory was propagated through the specified*

target–substrate geometry, and particles intersecting the substrate were recorded. Moreover, the incidence angles from all cells were grouped into 2° bins. The same binning and normalization procedures were applied to all independent runs for both configurations. The simulation results are discussed in Section 4.1.

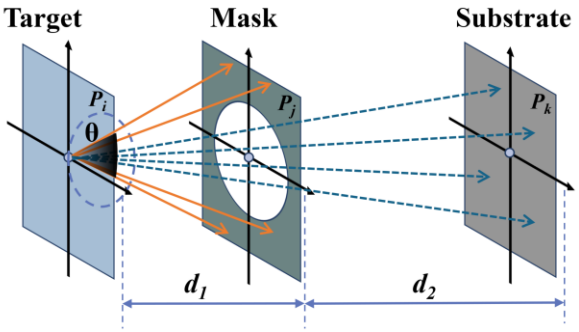


Figure.1. The schematic diagram of the target particle sputtering trajectory in Monte Carlo simulation.

3. Experimental

The Fe/Si multilayers were fabricated by using linear DC magnetron sputtering with honeycomb mask to explore its effect on the surface, interface, and magnetic properties. Fig. 2 showed the deposition masks in the practical linear DC magnetron sputtering process. *Vickery et al. investigated six honeycomb collimators with different geometries for W/Si multilayer deposition [14]. They found that preventing particles with incidence angles above about 50° from reaching the substrate kept the interfacial roughness low at about 3.5 Å, whereas allowing these large-angle particles to reach the substrate significantly increased the roughness. This study supported our selection of honeycomb mask parameters and provides guidance for future optimization.* As shown in Fig. 2(a), the correction mask was placed between the target and the substrate. It was used to improve the vertical uniformity of multilayer. *In Fig. 2(b), the honeycomb mask was introduced at a distance of 40 mm in front of the substrate, with its position aligned with that of the simulated region.* The length and width of Fe and Si target were 380mm and 130mm. The multilayers were deposited on a polished Si (100) crystal substrate with the size of 20 mm × 20 mm and the thickness of 0.5 mm. The base pressure before the deposition was 1.2×10^{-4} Pa. During the deposition process, high-purity (99.99%) Ar gas was inflated as the sputtering gas. The working pressure was maintained at 1.0 mTorr and the gas flow rate was 5 sccm. The sputtering power of the Fe target and the Si target was 250W and 300W respectively. *The distance between substrate and Fe target was 11.5 cm, while it was 11.5 cm for Si target.* The Fe/Si multilayer that fabricated without honeycomb mask was symbolized as S1 (N=12), while that with the honeycomb mask was symbolized as S2 (N=12). The bilayer thickness of sample S1 and S2 was 9.75 nm and 9.59 nm respectively. The ratio of Fe layer to the bilayer thickness ($\Gamma_{Fe} = d_{Fe}/d$) was 0.77 in

S1, while the ratio was 0.79 in S2. *The two samples were designed as a controlled pair to evaluate the effect of the honeycomb mask. The Fe and Si layer thicknesses in both samples correspond to the thinnest bilayer in an (m=3) Fe/Si neutron polarizing supermirror. These thin bilayers mainly affect the reflectivity near the upper critical edge at high (q), where interface quality is particularly important.* The thickness control of each layer was realized by varying the substrate speed through the sputtering region. The preparation parameters of the two samples were kept the same. The honeycomb mask limited the large-angle incident particles for S2, so its thickness was slightly decreased.

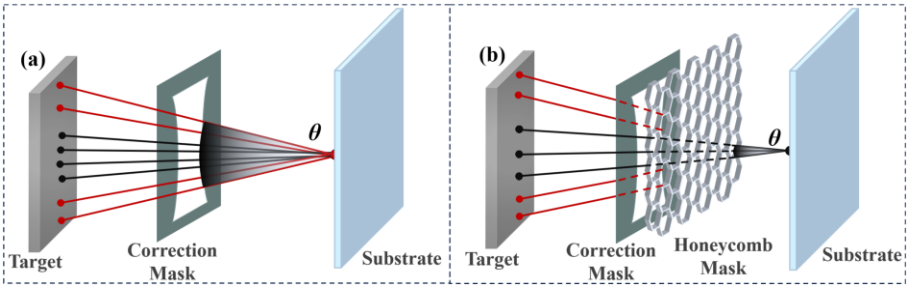


Figure.2. DC magnetron sputtering. (a) without honeycomb mask (S1) and (b) with honeycomb mask (S2).

The surface and interface performance were charactered with Grazing incidence X-ray reflectivity (GIXR), AFM, optical profilometer (OP), X-ray diffuse scattering (XRS), and XRD. GIXR and XRS were employed to characterize the interfacial properties of multilayers, utilizing a Bruker D8 Discover X-ray diffractometer furnished with a Cu-Kα radiation source at the wavelength of 0.154nm (8.04 keV). The GIXR measurements were carried out by a specular scan mode (θ-2θ) with the range of $0°<2\theta<8°$ [22]. The layer thicknesses, densities, and interface widths of the Fe/Si multilayers were obtained by fitting the GIXR curves with GenX software [23]. The XRS were measured with a rocking-scan mode, where the incident and detector angles scanned around the first Bragg peak of the GIXR curve. The XRS curves were fitted using IMD software [24] for the interface roughness, interfacial diffusion, and lateral correlation length. In addition, XRD curves were measured to analyze the crystalline phases in the layers, using a Bruker D8 DISCOVER diffractometer with Cu Kα radiation ($\lambda = 0.154$ nm) in a θ–2θ scan mode. OP and AFM were employed to characterize the surface roughness of Fe/Si multilayers. AFM tests were performed in tapping mode via a Bruker Dimension Edge system, covering three fields of view (FOV) of 1 μm × 1 μm, 5 μm × 5 μm, and 10 μm × 10 μm. OP tests were carried out using a Bruker Contour GT-X3), with two FOV: 624 μm × 468 μm and 125 μm × 94 μm. Magnetic properties were critical in governing the polarization performance of neutrons. To characterize the magnetization behavior of the samples, the coercivity (H_c) was tested by using a vibrating-sample magnetometer (LAKESHORE 7407). *However, their neutron-optical performance has not yet been directly assessed. Future work will employ polarized neutron reflectometry (PNR) to*

determine the nuclear and magnetic scattering-length-density profiles and to evaluate the polarization reflectivity and polarization efficiency.

4. Result and discussion

4.1. Simulation Results of Particle Incidence Angle Distribution

To improve the statistical stability of the simulation, the Monte Carlo run was performed for each configuration, with and without the honeycomb mask. Particle-number convergence was examined using N=100000, N=300000, N=500000, N=1000000 particles for both configurations, as shown in Fig. 3. The particles were generated from random positions on the target surface according to the angular probability model described above. The entire 300 mm × 200 mm substrate was divided into 2400 cells of 5 mm × 5 mm. These cells recorded the landing positions and incidence angles of particles reaching the substrate. The incidence angles collected from all cells were binned into 2° intervals. The simulated incidence-angle distributions were shown in Fig. 3. The target–substrate geometry affected the incidence angles of particles reaching the substrate. Consequently, the distributions for both configurations peaked between 40° and 50°. For all particle numbers examined, the incidence-angle distribution extended from approximately 0° to 73° without the honeycomb mask, whereas it was restricted to approximately 0°–52° after the honeycomb mask was introduced, as shown in Fig. 3(a)–(d). The honeycomb mask did not collimate all particles along the substrate normal. Instead, it mainly blocked particles that would otherwise reach the substrate at incidence angles above 52°. As shown in Fig.3, increasing the particle number reduced the sampling fluctuations, whereas the overall incidence-angle distributions remained essentially unchanged. Increasing the number of simulated particles from 100000 to 1000000 reduced random sampling fluctuations and improved the stability of the calculated distributions. The overall incidence-angle distributions remained nearly unchanged as the number of simulated particles increased. This result confirms that the honeycomb mask reduced the fraction of large-angle incident particles through geometric filtering.

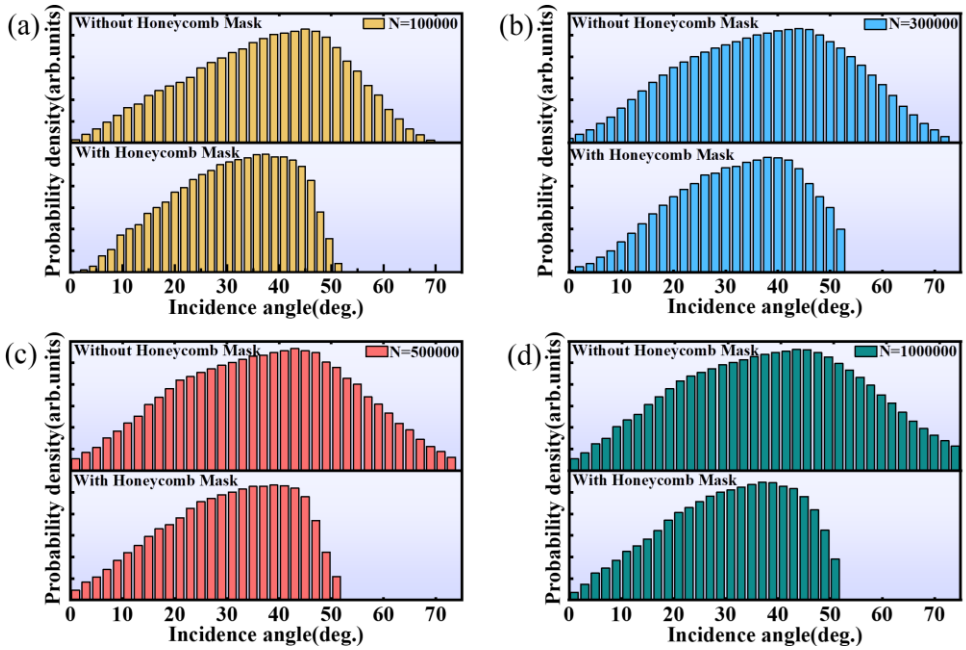


Figure.3. Monte Carlo-simulated incidence-angle distributions for different numbers of particles: (a) N=100000, (b) N=300000, (c) N=500000, and (d) N=1000000. The upper and lower histograms in (a)–(d) correspond to without and with the honeycomb mask, respectively.

4.2. Interface Width according to GIXR Analysis

As shown in Fig. 4, the measured and fitted GIXR curves were presented for the Fe/Si multilayers deposited with and without the honeycomb mask under otherwise identical conditions. The Bragg peaks of S1 and S2 occurred at nearly the same angular positions, indicating similar bilayer thicknesses. The GIXR curves were fitted using the differential-evolution algorithm implemented in GenX [23]. In the structural model, the top Si layer and bottom Fe layer were modeled separately, while the intermediate 11 Fe/Si bilayers were treated as a repeated stack. The fitted densities of Fe and Si remained close to their respective bulk values of 7.874 and 2.330 g cm^{-3} [29-30]. The fitted curves reproduced the main features of the measured curves, including the Bragg-peak positions and overall intensity profiles, as shown in Figure 4. The Fe and Si layer thicknesses, densities, and effective interface widths obtained from the GIXR fitting were summarized in Table 1. The two interfaces were distinguished according to the deposition sequence. The Fe-on-Si interface was formed when Fe was deposited onto an underlying Si layer, whereas the Si-on-Fe interface was formed when Si was deposited onto an underlying Fe layer. The effective interface width was defined as the Gaussian root-mean-square width of the laterally averaged electron-density transition across an interface in the GenX model [23]. Because specular GIXR cannot distinguish morphological roughness from compositional grading caused by interdiffusion, the fitted interface width represented the combined contribution of both effects [31-32]. For S1, the effective interface widths of the Fe-on-Si and Si-on-Fe

interfaces were 0.79 and 0.57 nm, respectively. For S2, the corresponding values decreased to 0.53 and 0.45 nm, respectively. Interface roughness and interdiffusion were further discussed in Section 4.4 based on the X-ray scattering results. These results demonstrated that the effective widths were decreased by using honeycomb mask.

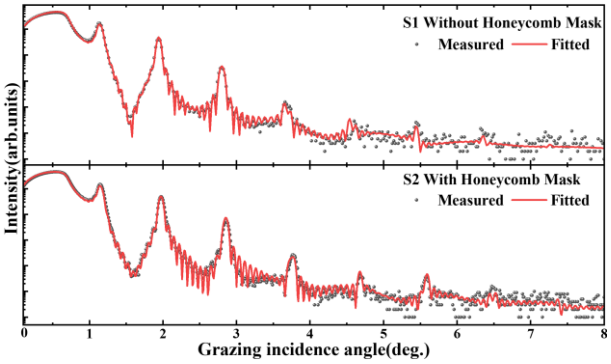


Figure.4. GIXR curves (black circles) and the fitting results (red solid lines) for Fe/Si multilayers without and with honeycomb mask.

Table 1. Structural parameters of Fe/Si multilayers deposited with and without honeycomb mask obtained from fitting the GIXR curves

Sample	**N**	***d*(nm)**	d_{Fe}**(nm)**	d_{Si}**(nm)**	$\sigma_{Fe-on-Si}$**(nm)**	$\sigma_{Si-on-Fe}$**(nm)**
S1	12	9.77	7.57	2.20	0.79	0.58
S2	12	9.60	7.53	2.07	0.53	0.45

4.3. Surface Roughness by using OP and AFM

The surface morphologies of S1 and S2 were measured by AFM and OP as shown in Fig. 5. Surface morphologies scanned by AFM in 1 μm×1 μm FOV were presented in Fig. 5(a) and (b). The surface morphology of S2 with the honeycomb mask exhibited the roughness of 0.16 nm RMS and 1.1 nm peak-to-valley (PV). In contrast, the S1 without the honeycomb mask showed more isolated protrusions. The roughness was 0.29 nm RMS and 1.4 nm PV. Fig. 5(c) and 5(d) showed OP surface morphology images of Fe/Si multilayers deposited using without and with the honeycomb mask in 125 μm × 94 μm FOV. Obtained roughness was 0.39 nm RMS for S2 and 0.67 nm for S1. The introduction of the honeycomb mask during deposition was confirmed to reduce the surface roughness of the Fe/Si multilayers.

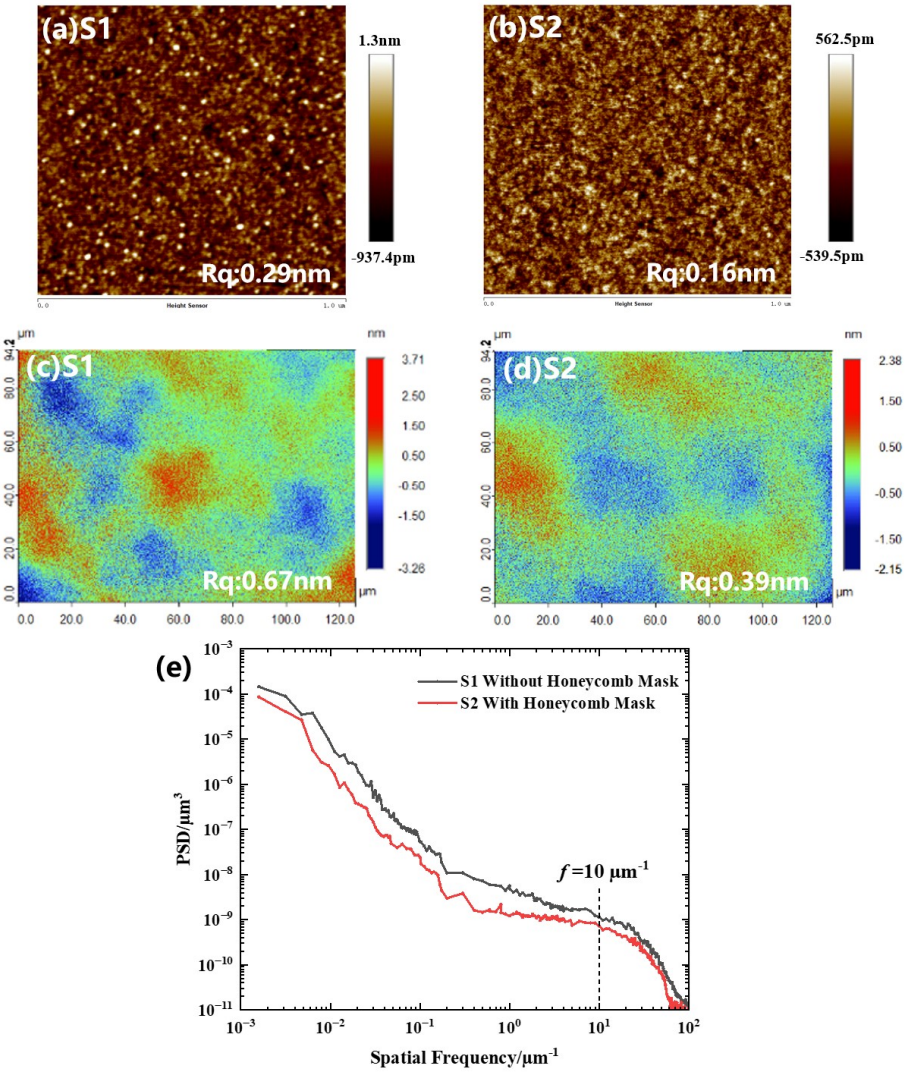


Figure 5. Surface morphology images of Fe/Si multilayer (a) without honeycomb mask and (b) with honeycomb mask, measured using AFM in 1 um × 1 um FOV; (c) without honeycomb mask and (d) with honeycomb mask, measured by OP in 125 μm × 94 μm FOV. (e) The one-dimensional power spectral density (PSD) of surface morphology.

The surface morphology comparison of each frequency was achieved by the power spectral density (PSD) analysis. The OP images in 624 μm × 468 μm and 125 μm × 94 μm FOV, as well as the AFM images in 1 μm × 1 μm, 5 μm × 5 μm, and 10 μm × 10 μm FOV, were used for Fourier transformed and stitched. The PSD curves ranging from 2.0×10^{-2} μm^{-1} to 1.0×10^{2} μm^{-1} were obtained as presented in Fig. 5(e).

After adopting honeycomb mask, the PSD values decreased almost throughout the entire range. In the low-spatial-frequency range, the PSD curves of S1 and S2 were nearly parallel. In the low-spatial-frequency range, the PSD curves of S1 and S2 were nearly parallel. The lower PSD values

of S2 suggested that both samples had a similar frequency dependence of the large-scale morphology, but S2 had smaller surface-height fluctuations [33-34]. Spatial frequency was related to spatial wavelength by $\lambda_s = 1/f$. *Therefore, the high-spatial-frequency region of* $f > 10\ \mu m^{-1}$ *corresponded to lateral wavelengths smaller than* $\lambda_s < 0.1\ \mu m$ *and primarily represents fine-scale surface features resolved by the small-FOV AFM measurements [31]. In the high-spatial-frequency range, the lower PSD level of S2 was associated with roughness at small FOV, consistent with the decrease in the AFM (1* μm*) value from 0.29 to 0.16 nm. For S1, more large angle particles reached the surface protrusions, while fewer reached the recessed regions because of geometric shadowing. This difference in particle flux increased local height variations and surface roughness. The honeycomb mask reduced the large angle particle flux and weakened the shadowing effect. As a result, deposition became more uniform at short lateral length scales, leading to lower PSD values in the high-frequency range [35-36]. Overall, the decreases in the PSD level and surface roughness were consistent with the AFM, OP, and GIXR results.*

4.4. Interface Roughness by using XRS analysis

Although the surface morphologies by using AFM and OP showed the significantly reduced surface roughness with honeycomb mask, they cannot represent the interface roughness quantitatively. The above GIXR curves could be used to calculate the interface width of Fe/Si multilayers, but the contributions of interface roughness (σ_r) and interface diffusion (σ_d) cannot be isolated from the interface width. Therefore, XRS curves were measured near the first Bragg peak of the GIXR curve to obtain the interface roughness. They were normalized using the maximum intensity, as shown in Fig. 6. The honeycomb-hole mask significantly reduced the diffuse reflection intensity of the S2, which was consistent with the report of Vickery et al [14].

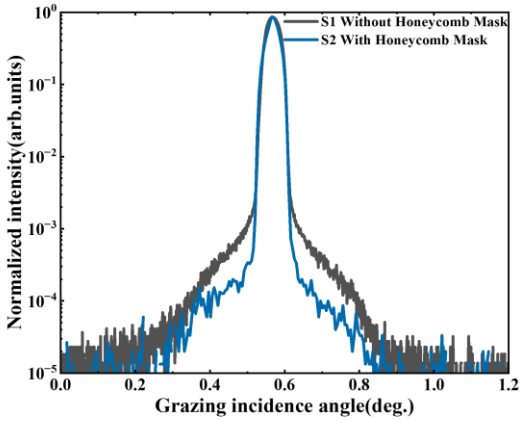


Figure.6. XRS curves (rocking curves) of Fe/Si multilayers deposited without and with honeycomb mask around 1st Bragg peaks (~0.55° grazing).

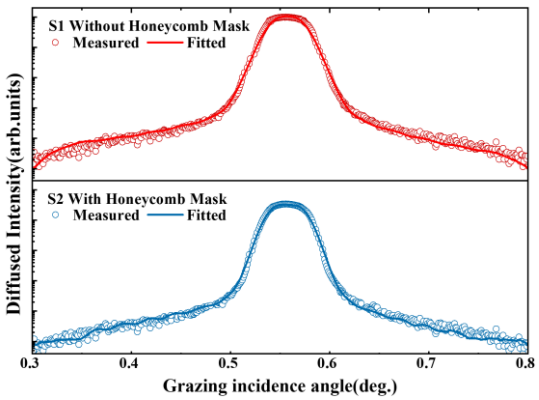


Figure.7. XRS curve fitting results of Fe/Si multilayers deposited without and with honeycomb mask around 1st Bragg peaks (~0.55° grazing).

The interface roughness was obtained by quantitatively analyzing XRS curves in IMD software with first-order distorted-wave Born approximation (DWBA). In this fitting model, each multilayer interface was described by a power spectral density (PSD) function [37-38]. The PSD was defined by the interface roughness σ_r, the in-plane lateral correlation length $\xi_{||}$, and the sawtooth factor h. These parameters were determined by the intrinsic properties of the multilayer system. The value range of sawtooth factor h was from 0.5 to 1. For smooth sputter-deposited multilayers, h was typically set to [39-41]. The XRS curves and corresponding fitting curves were compared in Fig. 7. Subsequently, the interface widths (σ) were obtained, which were contributed by interfacial diffusion (σ_d) and interface roughness (σ_r) as $\sigma^2 = \sigma_r^2 + \sigma_d^2$ [40-41]. The interface diffusion (σ_d) was subsequently determined from the value of σ_r. The obtained interface parameters were listed in Table 2, consistent with those via fitting GIXR. The interface roughness of Fe-on-Si interfaces was higher than that of Si-on-Fe. It could be attributed to the difference in surface free energy between Fe and Si (Si: 1.2 J/m²; Fe: 2.9 J/m²) [41]. In Fe/Si multilayers, island-like agglomerative growth could be facilitated by high surface free energy and rapid interlayer diffusion of Fe. Such phenomena increased interlayer, surface roughness and interface widths. In contrast, the Si layers remained comparatively smaller interface roughness [5,6,42]. Meanwhile, the interface roughness values obtained through fitting XRS were similar to the interface widths via GIXR, indicating that interface roughness dominated the interfacial characteristics. *After introducing the honeycomb mask, the Fe-on-Si and Si-on-Fe interface roughness values decreased from 0.71 and 0.50 nm to 0.47 and 0.40 nm, respectively. This reduction was attributed to the suppression of large-angle incident particles and the resulting decrease in deposition-induced interface fluctuations.*

The lateral coherence length was consistent with the interfacial morphological features of the film interfaces: a larger lateral coherence length corresponds to a larger lateral correlation scale of the roughness [43]. Compared with S1, the lateral coherence lengths at both the Fe-on-Si and Si-on-Fe

interfaces were reduced in S2. *The lower lateral correlation length of S2 shows that the interface-height variations were correlated over a shorter distance. Together with the lower interface roughness, this suggests that the honeycomb mask reduced large-scale roughness features. This result further supports the effect of the honeycomb mask on improving the interface morphology. Meanwhile, the cumulation of bilayers led to higher surface roughness [44-46]. Although GIXR, XRS, AFM, and OP probe different structural features and length scales, all measurements showed consistent reductions in interface width, interface roughness, and surface roughness.*

Table2. The XRS fitting parameters of Fe/Si multilayer samples without and with honeycomb mask. Here, σ represents the interface fitting value from GIXR.

Sample	**N**	**Fe-on-Si**				**Si-on-Fe**			
		$\boldsymbol{\sigma(nm)}$	$\boldsymbol{\sigma_r(nm)}$	$\boldsymbol{\sigma_d(nm)}$	$\boldsymbol{\xi_{\|\|}(nm)}$	$\boldsymbol{\sigma(nm)}$	$\boldsymbol{\sigma_r(nm)}$	$\boldsymbol{\sigma_d(nm)}$	$\boldsymbol{\xi_{\|\|}(nm)}$
S1	12	0.79	0.71	0.35	1305.6	0.58	0.50	0.31	990.5
S2	12	0.53	0.47	0.25	1005.6	0.45	0.40	0.21	780.5

4.5. X-ray Diffraction

To evaluate the crystallization characteristics of the Fe/Si multilayers, XRD measurements were carried out on the S1 and S2 samples using a Bruker D8 Advance diffractometer. The crystalline phases were identified by comparing the measured XRD patterns with the reference powder diffraction file (PDF) data from the International Centre for Diffraction Data (ICDD) using JADE software. As shown in Fig. 8, both samples exhibited a broad diffraction peak near 2θ = 44.67°, which was assigned to bcc-Fe (110) (PDF No. 50-1275). No additional diffraction peaks were observed, indicating that the honeycomb mask did not change the crystalline phase of the Fe layers. For quantitative comparison, the Fe (110) peaks of both samples were fitted over the same angular range using an identical pseudo-Voigt function and background model. The fitted curves adequately reproduced the peak positions, widths, and overall profiles of the Fe (110) peaks. Minor differences between the measured and fitted curves were mainly observed in the low-intensity background regions, particularly on the high-angle side of the S2 pattern. However, no clear systematic deviation was observed in the main peak region. Therefore, the fitting was considered adequate for extracting and comparing the peak positions and FWHM values of the two samples. The fitted peak positions were 44.67°±0.02° for S1 and 44.67°±0.05° for S2. The corresponding FWHM values were 1.35°±0.07° for S1 and 1.43°±0.07° for S2, respectively. The reported uncertainties represent one standard error obtained from the nonlinear least-squares peak fitting [47]. The average crystallite sizes were calculated from the fitted FWHM values of the Fe (110) peaks using the Scherrer equation. The apparent crystallite sizes were approximately 6.5 ± 0.3 nm for S1 and 6.0 ± 0.3 nm for S2. The

uncertainties represent a minimum model-related uncertainty of about 5% associated with the use of fitted peak widths in the Scherrer equation [48]. The difference of approximately 0.5 nm between the two samples was comparable to the estimated uncertainty. Therefore, no clear change in the Fe crystallite size was identified after introducing the honeycomb mask. In contrast, Zubayer et al. recently reported that incorporating 14 vol.% $^{11}B_4C$ into both the Fe and Si layers produced a nearly fully amorphous multilayer, whereas pure Fe/Si multilayers showed clear crystallinity [1]. The incorporation of $^{11}B_4C$ suppressed Fe crystallite growth and iron-silicide formation, thereby reducing the interface width and diffuse scattering. Thus, the $^{11}B_4C$ approach improves interface quality mainly through composition-induced amorphization. In the present study, the honeycomb mask improved the surface and interface quality by limiting large-angle incident particles and weakening the geometric shadowing effect. It did not change the material composition or Fe crystal structure. Therefore, these two approaches improve multilayer quality through different mechanisms. These results suggest that the improvements in surface and interface quality were unlikely to originate from a change in Fe crystallization.

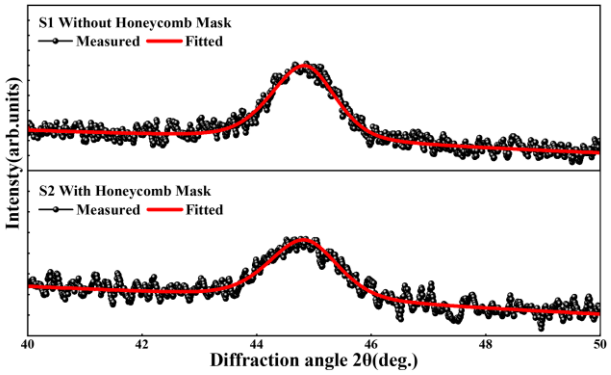


Figure 8. XRD results of Fe/Si multilayer samples (a) without honeycomb mask and (b) with honeycomb mask

4.6. Hysteresis loop measurement

As discussed above, the honeycomb mask reduced the interface width, interface roughness, and surface roughness of the Fe/Si multilayers. To examine whether these structural improvements affected their magnetic response, in-plane hysteresis loops were measured, as shown in Fig. 9. Hysteresis loops were measured with the applied magnetic field oriented parallel and perpendicular to the film plane. Each sample was carefully aligned before measurement. For the in-plane measurements, the film plane was aligned parallel to the applied field, whereas for the out-of-plane measurements, the film normal was aligned parallel to the field. The absolute angular uncertainty of the measurement system was approximately ± 1°. Previous studies have shown that a sample misalignment of approximately 1° can introduce spurious features into hard-axis magnetization curve [49]. S1 and S2

were measured using the same sample holder, alignment reference, and measurement protocol, with the relative difference between their mounting angles controlled within 0.1°. Therefore, the hysteresis loop test results of S1 and S2 can be reliably compared.

For the testing of hysteresis loops parallel to the plane, S1 exhibited a saturation magnetization (M_s) of 1136 emu/cm³ and a coercivity (H_c) of 50 Oe, whereas S2 exhibited an M_s of 1187 emu/cm³ and an H_c of 25 Oe. Thus, the use of the honeycomb mask was accompanied by a slight increase in M_s and a decrease in H_c. The lower H_c of S2 is consistent with its reduced interface and surface roughness because morphological irregularities may act as pinning sites for domain-wall motion [50-51]. Overall, limiting large-angle incident particles improved the interface and surface quality without compromising the ability of the Fe/Si multilayers to reach in-plane magnetic saturation. For the perpendicular hysteresis-loop measurements, previous studies have shown that deposition at large or oblique incidence angles enhances the self-shadowing effect and may promote the growth of directional or tilted columnar microstructures [52]. The resulting shape anisotropy can cause the local easy axes to deviate from the film plane [49,53]. Therefore, the more pronounced out-of-plane magnetization response of S1 may be associated with the growth-induced anisotropy and higher roughness caused by large-angle incident particles. By contrast, the honeycomb mask reduced the fraction of large-angle incident particles and decreased the surface and interfacial roughness of S2, thereby weakening the associated structure-induced anisotropy and its out-of-plane magnetization response.

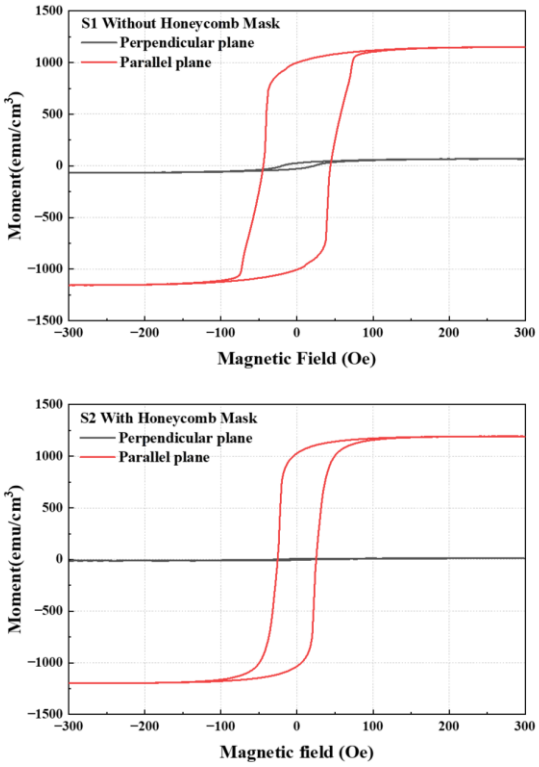


Figure 9. Magnetization hysteresis loops of Fe/Si multilayer deposited (a) without honeycomb mask and (b) with honeycomb mask.

5. Conclusion

This paper focuses on reducing the interface roughness of Fe/Si multilayers by introducing *the honeycomb mask* to limit large-angle incident particles, including *incidence angle* distribution simulation, roughness characterization, and the magnetic properties of Fe/Si multilayers.

(1) The honeycomb mask was designed to limit the large-angle incident particles. The angle distributions of incident particles were obtained by the Monte Carlo simulations. Without the honeycomb mask, the incidence angles ranged approximately from 0 to 73°. After adopting the honeycomb mask, the range was narrowed down to about 0 to 52°. It clearly demonstrated that the honeycomb mask limited large-angle incident particles.

(2) The Fe-on-Si/Si-on-Fe interface widths decreased from 0.79/0.57 nm to 0.53/0.45 nm by fitting GIXR curves. The surface roughness was reduced to RMS 0.16 nm in AFM and 0.39 nm in OP by using honeycomb mask, compared with the sample without honeycomb mask (RMS 0.29 nm in AFM and 0.67 nm in OP). The Fe-on-Si/Si-on-Fe interface roughness decreased from 0.71/0.50 nm to 0.47/0.40 nm by fitting XRS curves. *The experimentally observed reductions in interfacial width, surface roughness, and interfacial roughness were associated with the reduced incidence of large-angle particles, in agreement with the Monte Carlo simulation results.*

(3) The further effect on magnetic properties were obtained by using hysteresis loops. According to the in-plane magnetic hysteresis loops, a higher M_s was achieved by using honeycomb mask (from 1136 emu/cm³ to 1187 emu/cm³). The *cc* was lower (from 50 Oe to 25 Oe). Moreover, this change caused only by interface roughness reduction, because the crystallite size remained essentially unchanged according to XRD results.

For neutron supermirrors, the thinner bilayers contribute primarily to the reflectivity near the upper critical edge, where interface quality is particularly important. The honeycomb mask reduces the number of particles reaching the substrate at large incidence angles. This reduces the interfacial width and roughness of the thin Fe/Si bilayers and lowers the surface roughness of the multilayer. The improved interface and surface quality may suppress interdiffusion and off-specular scattering. Consequently, reflectivity losses may be reduced. This method therefore has the potential to improve the high-(q) reflectivity of Fe/Si neutron polarizing supermirrors. Future work will apply the honeycomb mask to supermirror fabrication and evaluate its effectiveness through neutron reflectivity and polarization-efficiency measurements.

Acknowledgments

This work was supported by the Key Program of National Natural Science Foundation of China (12335018).

References

[1] Causer G L, Guasco L, Paull O and Cortie D 2023 *Phys. Status Solidi RRL* **17** 2200421

[2] Ashkar R, Bilheux H Z, Bordallo Het al.2018 *Acta Crystallogr*. D **74** 1129

[3] Barker J, Moyer J, Kline S, Jensen G, Cook J, Gagnon C, Kelley E, Chabot J P, Maliszewskyj N, Parikh C, Chen W, Murphy R P and Glinka C 2022 J. *Appl. Crystallogr*. **55** 271

[4] Xue Z L, Ramirez-Cuesta A J, Brown C M, Calder S, Cao H, Chakoumakos B C, Daemen L L, Huq A, Kolesnikov A I, Mamontov E, Podlesnyak A A and Wang X 2019 *Eur. J. Inorg. Chem*. **2019** 1065

[5] Zhang Z, Wang J J, Lian Y H, Alnaimi R, Wang Z S and Chen H 2015 *Thin Solid Films* **592** 312

[6] Kumar A, Brajpuriya R and Singh P 2018 *J. Appl. Phys.* **123** 025305

[7] Ashfaq A and Stahn J 2009 *Appl. Surf. Sci.* **255** 5902

[8] Kharmouche A and Bensehil I 2019 *J. Mater. Sci.: Mater. Electron.* **30** 631

[9] Høghøj P, Anderson I, Siebrecht R, Graf W and Ben-Saidane K 1999 *Physica B* **267-268** 355

[10] Zubayer A, Eriksson F, Falk M, Lorentzon M, Palisaitis J, Klauser C, Nagy G, Wolf P M, Pitthan E, Holeňák R, Primetzhofer D, Stenning G B G, Glavic A, Stahn J, Dorri S, Eklund P, Birch J and Ghafoor N 2025 *J. Phys. Chem. C* **129** 7921

[11] Aldimassi A M, Chevalier A, Ben Youssef J, Laur V and Rouvellou B. 2020 *AIP Adv* 10, 065218

[12] Sun S, Yu B, Guo T, Yao S, Liu Y, Deng W, Li C and Jin C. 2020 *Optics Express* 28 1351

[13] Messier R, Giri A P and Roy R A 1984 *J. Vac. Sci. Technol. A* **2** 500

[14] Vickery A, Jensen C P, Christensen F E, Steenstrup M P and Schønfeldt T 2008 *X-Ray Opt. Instrum.* **2008** 792540

[15] Li J, An Q and Fang H 2024 *Appl. Surf. Sci.* **646** 158914

[16] Deng L 2022 *High Power Laser Part. Beams* **34** 026001 (in Chinese)

[17] Shi Y, Huang Q, Qi R, Shen Z, Zhang Z and Wang Z 2020 *Coatings* **10** 357

[18] Westwood W D 1978 *J. Vac. Sci. Technol.* **15** 1

[19] Ekpe S D, Bezuidenhout L W and Dew S K 2005 *Thin Solid Films* **474** 330

[20] Broadway D M, Platonov Y Y and Gomez L A 1999 *Proc. SPIE* **3766** 262

[21] Vossen J L 1974 *J. Vac. Sci. Technol.* **11** 875

[22] Wormington M, Panaccione C, Matney K M and Bowen D K 1999 *Philos. Trans. R. Soc. A* **357** 2827

[23] Glavic A and Björck M 2022 *J. Appl. Crystallogr.* **55** 1063

[28] Windt D L 1998 *Comput. Phys.* **12** 360

[29] Haynes W M (ed.) 2014 *CRC Handbook of Chemistry and Physics*, 95th edn. (Boca Raton, FL: CRC Press) pp. 2–4

[30] United States Superintendent of Documents 1992 *National Institute of Standards and Technology (Subject Bibliography)* (Washington, DC: U.S. Government Printing Office) pp. 1–20

[31] Gawlitza P, Braun S, Lipfert S and Leson A 2006 *Proc. SPIE* **6317** 63170G

[32] Tanner B K 2018 Grazing Incidence X-Ray Reflectivity and Scattering, *in Handbook of Advanced Non-Destructive Evaluation*, ed Ida N and Meyendorf N (Cham: Springer) pp. 1-34

[33] Spiller E, Baker S L, Parra E and Tarrio C 1999 *Proc. SPIE* **3767** 143

[34] Jacobs T D B, Junge T and Pastewka L 2017 *Surf. Topogr.: Metrol. Prop.* **5** 013001

[35] Duparré A, Ferre-Borrull J, Gliech S, Notni G, Steinert J and Bennett J M 2002 *Appl. Opt*. **41** 154

[36] Rechendorff K, Hovgaard M B, Chevallier J, Foss M and Besenbacher F 2005 *Appl. Phys. Lett*. **87** 073105

[37] Holý V and Baumbach T 1994 *Phys. Rev. B* **49** 10668

[38] Stearns D G, Gaines D P, Sweeney D W and Gullikson E M 1998 *J. Appl. Phys.* **84** 1003

[39] Abharana N, Biswas A, Sarkar P, Rai S, Singh S, Kumar S, Jha S N and Bhattacharyya D 2019 *Vacuum* **169** 108864

[40] Sarkar P, Biswas A, Ghosh S K, Rai S, Modi M H and Bhattacharyya D 2020 *Thin Solid Films* **693** 137688

[41] Sarkar P, Biswas A, Rai S, Srivastava H, Mandal S, Modi M H and Bhattacharyya D 2020 *Vacuum* **181** 109610

[42] Gupta A, Kumar D and Phatak V 2010 *Phys. Rev. B* **81** 155402

[43] Savage D E, Schimke N, Phang Y H and Lagally M G 1992 *J. Appl. Phys.* **71** 3283

[44] Wang Z, Li T, Zhang Z, Chang C, Xia J, Zhang Z, Jiang L, Qi R, Huang Q, Zhang Z and Wang Z 2024 *Vacuum* **230** 113750

[45] Freitag J M and Clemens B M 2001 *J. Appl. Phys.* **89** 1101

[46] Fullerton E E, Pearson J, Sowers C H, Bader S D, Wu X Z and Sinha S K 1993 *Phys. Rev. B* **48** 17432

[47] Cancellieri C, Lorenzin G, Unutulmazsoy Y, Lotnyk A and Ariosa D 2025 *J. Appl. Crystallogr*. **58** 1995

[48] Noyan I C and Öztürk H 2022 *J. Appl. Crystallogr*. **55** 455

[49] Hindmarch A T, Suszka A K, MacKenzie M, Chapman J N, Henini M, Taylor D, Hickey B J and Marrows C H

2009 *J. Appl. Phys.* **105** 073907

[50] Lin W C, Ho T Y, Chi C S and Tsai C J 2013 *Thin Solid Films* **542** 355

[51] Zhao Y P, Gamache R M, Wang G C, Lu T M, Palasantzas G and de Hosson J T M 2001 *J. Appl. Phys.* **89** 1325

[52] Chowdhury N and Bedanta S 2014 *AIP Adv*. **4** 027104

[53] Pires M J M, Araújo Filho M S, Tedesco J C G, Ardisson J D and Macedo W A A 2014 *J. Phys. Chem. Solids* **75** 1124